Seismic numerical analysis of an Inca stone wall in Sacsayhuaman using rigid body dynamics within a finite element framework

Leonel Lipa[1,3], Nicola Tarque[2,1,*], Luca Pelà[3] and José María Goicolea[2]

[1]Gerdis Group, Civil Engineering Division, Pontificia Universidad Católica del Perú, Av. Universitaria 1801, Lima, Peru
[2] Department of Continuum Mechanics and Structures - E.T.S.I Caminos, Canales y Puertos, Universidad Politécnica de Madrid, C. Prof. Aranguren 3, 28040 Madrid, Spain
[3] Department of Civil and Environmental Engineering, Universitat Politècnica de Catalunya, Jordi Girona 1-3, 08034 Barcelona, Spain

Abstract. The study and conservation of the stone heritage is a global concern, mainly when the buildings are in seismic zones. Stone structures can be very simple or considerably complex, depending on their style and form of construction. A clear example is the Inca architecture in Peru, which has different and complex typologies due to its cultural diversity. Inca structures of remarkable heritage value are in Cusco, an area of active cortical faults that might produce a seismic event at any time. The main objective of this research is to contribute to the knowledge of the seismic vulnerability analysis of Inca's stone walls by using the dynamics of rigid bodies (within the finite element method) to evaluate the possible out-of-plane failure mechanisms. This methodology allows for reducing the high number of degrees of freedom usually considered when modelling an entire irregular large stone wall by other approaches, such as continuum models. A wall section from the archaeological site of Sacsayhuaman (Cusco, Peru) is analysed as a case study. Each stone is discretised and modelled as a rigid body, and the interaction among blocks is evaluated within a finite element numerical framework. The structure's predominant frequencies are evaluated using updated methods such as white noise and sinusoidal signals. Then, a non-linear dynamic analysis of the studied wall is performed considering three Peruvian seismic records. The analyses show that the structure could suffer significant damage and endanger its structural stability for cortical earthquakes with a Peak Ground Acceleration (PGA) greater than 0.2 g. Considering the historical significance of these structures, the analysis of Inca stone walls' seismic safety accounts for potential residual movements between individual stones.

Keywords: Dynamics of rigid bodies, Inca stone wall, finite element analysis, collapse mechanisms, earthquake.

1. Introduction

Dry-stone walls have existed since the beginning of humanity and are currently found in different countries worldwide. Most of these ancient constructions now belong to the World Heritage; however, some are prone to collapse due to environmental conditions, age, and lack of maintenance [1]. For these reasons, only a small part of the architectural heritage of the past exists, and we must preserve these constructions to allow future generations to know our cultural identity [2]. In Peru, stone structures have been built since its beginnings, such as in the Caral culture, one of the five most important civilisations on the planet and the oldest in America. In Caral, the inhabitants cut millions of stones they later brought to their city to construct their buildings [3]. However, the Inca culture made the most symbolic stone constructions in Peru because various stone structures enjoy hermeticity, complexity, and architectural beauty [4]. The Inca culture had the city of Cusco as its capital, and most of its symbolic structures are in this region. The airtightness of the Inca walls was achieved by carving the stones, generally of cyclopean size, and placing them one on top of the other so that they fit together without the use of mortar and with a precision that was often of the order of the fraction of a millimetre [5]. Unfortunately, several of these constructions have overturning problems due to settlements in the terrain or other external factors (*Figure 1*).

* Corresponding author

(a) (b) (c)

Figure 1. Structures with overturning problems in various archaeological sites in Cusco: (a) Pisaq, (b) Moray, and (c) Sacsayhuaman (Source: Andina.pe).

On the other hand, some authors indicate that the strong earthquakes in Cusco in 1650 or 1950, due to the geological faults in the area [6, 7], could have caused severe damage to various Inca constructions (Figure 2). These strong earthquakes have not been recorded since the first accelerometers were installed in Lima, Peru, in 1944 and 1972 [8].

(a) (b)

Figure 2. Existing damages in Inca structures in Cusco, possibly due to past earthquakes: (a) Coricancha Temple, and (b) Machupicchu.

Various researchers conducted experimental tests to understand the behaviour of stone structures based on real or reduced-scale specimens [9, 10, 11, 12, 13]. Dry joint stone walls were evaluated by numerical modelling using Finite Element Method (FEM) [9, 13], Discrete (or Distinct) Element Method (DEM), which refers to Smoothed Explicit Numerical Methods [11, 15, 17, 18] or a combination of them (FDEM) [19, 20]. In most of these analyses, the preparation of computer-aided 3D geometric models (CAD) is usually required to build numerical models due to the geometric complexity of elaborate shapes and morphology [21]. In FEM, the structure is divided into elements (sub-domains) and their stress state is evaluated based on continuum mechanics theory [22]. One of the main limitations of this method is that the model encounters significant difficulties in simulating large displacements between blocks [19], so they need ad-hoc contact laws to reproduce the discontinuities correctly. In DEM, the structure is idealised as discontinuous, in which the joints are modelled as surfaces following normal and tangential contact laws [23]. Spheres or sphere clumps are usually considered to simulate the elements to reduce computational time because the contact between 2 spheres is a point, and the normal direction of the contact plane is known [11, 24]. This process could be a disadvantage since, in various structures, the contact between ashlars is not a point but a surface. Jean M. and Moreau J.J. 's developments [16, 17, 18], known as contact dynamic methods, refine the discrete element method by tackling the problem differently. Instead of relying solely on positions and reaction forces at the end of each time step, it evaluates forces continuously throughout the step and considers relative velocities at the end. This shift to a more nuanced approach improves the representation of interactions between blocks in masonry structures, as it can handle blocks of any shape. In FDEM, FEM and DEM approaches are combined as the blocks are discretised into elements that follow continuum mechanics, while the joints follow surface contact laws [25]. Fracture and fragmentation are considered, and when they occur, contact interaction between the parts is considered [19, 26].

While FEM, DEM, and their combined form FDEM are powerful tools for analysing complex masonry

structures under seismic loads, particularly with non-linear dynamic analysis, they can be computationally demanding [27]. Among these, detailed FEM stands out for its accuracy in predicting earthquake behaviour of historical masonry structures. This approach provides exact details on deformations and damage patterns, allowing confident assessments of a structure's seismic resilience [28], but considering a high number of degrees of freedom.

On the other hand, the stones used for dry-joint structures can be idealised as rigid bodies [26, 29, 30] within the FEM since they have very high strength and stiffness. This modelling assumption leads to a considerable reduction of degrees of freedom and computational time, with consequent advantages in terms of calculation efficiency. Rigid bodies are elements that do not deform [31], so the distance between two points within each element remains constant, regardless of the external forces applied to it. Rigid body dynamics may be used within a finite element framework that follows contact laws at the joints to reproduce the development of large displacements.

Moreover, evaluating the overall structural response of a wall under dynamic loading is crucial. In various engineering fields, it can be measured by three possible approaches [32]: deformation-based [33], vibration-based [34], and wave-based [35]. The deformation-based approach allows the direct measurement of the interface deformation caused by either external loading or displacement. This deformation is associated with normal and tangential stresses and hysteretic energy losses at the interface. The vibration-based approach allows the measurement of vibration frequencies, vibration modes, and damping of a system by using dynamic identification techniques to estimate interface properties and behaviour. Finally, the wave-based approach is a non-invasive testing method assessing the transmission of waves between two bodies. This approach assumes that the normal and tangential stiffness is proportional to the longitudinal/transverse reflection coefficient, emission frequency, wave velocity, and material density.

This study uses advanced numerical methods to understand how geometrically complex dry-stone walls would respond to earthquakes. The methodology involves the finite element method, the dynamics of rigid body, and contact laws. Based on historical Peruvian seismic records, the study provides valuable insights into damage patterns for various earthquake intensities (peak ground accelerations or PGA), determining residual displacements and the collapse mechanisms of a section of an Inca's stone wall. In addition, a highly detailed 3D model of the wall section was created. The methodology and preliminary results contribute to the knowledge for reducing the seismic vulnerability of the stone buildings.

The research is organized as follows. Section 2 details some important concepts of the methods used. Then, Section 3presents an example of application of the numerical methodology by using the dynamics of rigid bodies, and comparison between experimental and numerical model. After validating the method, Section 4 presents an Inca wall section of the Sacsayhuaman site modelled in Abaqus software. The dominant frequencies of the wall are evaluated using white noise and sinusoidal signals (vibration-based approach). Numerical modelling was carried out in Abaqus, considering the stones as rigid bodies. The analysis of the collapsing mechanisms, stone displacements and damage patterns are evaluated in Section 5 through non-linear dynamic analyses. Peruvian seismic records give the input acceleration signals. Also, this Section compares and discusses the primary outcomes obtained from the numerical analyses. Finally, Section 6 summarizes the key findings of this research.

2. Rigid body dynamics and contact laws

2.1 Mechanical behaviour of rigid bodies

Rigid bodies are elements whose motion is controlled by a reference point, which, for convenience, is the mass centre [36]. Working with rigid bodies allows for a reduction of the degrees of freedom of the assembly and thus reduces the computational time. A rigid body has six degrees of freedom (DOFs), i.e. three DOFs that define the translation $\boldsymbol{u}_c$ (u_1, u_2, u_3) concerning the reference point, and three DOFs of rotation $\boldsymbol{\phi}$ (ϕ_1, ϕ_2, ϕ_3), that are components of the Euler's finite rotation vector and define the orientation. Finite rotations in dynamics are highly nonlinear and not as straightforward as translational DOFs. The increments of the rotation variables are calculated in Abaqus using the exponential of the rotation matrix [37, 38]. The incremental small displacements give rise to a skew-symmetric matrix, which is integrated for each time increment using an exponential mapping to produce the finite rotation matrix.

The relative positions of each node always remain constant, so they do not deform, allowing the body to undergo large displacements and rotations.

The strong or local form to solve the equilibrium of bodies is through Newton-Euler's linear and angular momentum principles (equations 1 and 2).

$$\boldsymbol{F} = m\ddot{\boldsymbol{u}}_c \tag{1}$$

$$\boldsymbol{M} = \mathrm{d}\boldsymbol{L}/\mathrm{d}t = \mathrm{d}(\boldsymbol{I}\cdot\boldsymbol{\omega})/\mathrm{d}t = \boldsymbol{I}\cdot\dot{\boldsymbol{\omega}} + \boldsymbol{\omega}\times\boldsymbol{I}\cdot\boldsymbol{\omega} \tag{2}$$

where $\boldsymbol{F}$ is the force resultant, m is the mass, $\boldsymbol{L}$ is the angular momentum, $\boldsymbol{M}$ is the torque resultant, $\boldsymbol{I}$ is the inertia tensor, $\boldsymbol{u}_c$ the translation of the rigid body, and $\boldsymbol{\omega}$ the angular velocity which is the derivative of vector $\boldsymbol{\phi}$.

Abaqus uses the weak or variational form of equilibrium, that is: $\delta W_{\text{int}} + \delta W_{\text{ext}} = 0$, in which the inertial contribution of the virtual work from each rigid body δW_{int} can be calculated with the D'Alembert principle at each time instant:

$$\delta W_{\text{int}} = -\int_V \rho\, \delta\boldsymbol{u}\cdot\ddot{\boldsymbol{u}}\, dV = -m\ddot{\boldsymbol{u}}_c\cdot\delta\boldsymbol{u}_c - (\boldsymbol{I}\cdot\dot{\boldsymbol{\omega}} + \boldsymbol{\omega}\times\boldsymbol{I}\cdot\boldsymbol{\omega})\cdot\delta\boldsymbol{\phi} \tag{3}$$

where $\delta\boldsymbol{u} = \delta\boldsymbol{u}_c + \delta\boldsymbol{\phi}\times r$, is the variation of the position at each point of the rigid body, and $\delta\boldsymbol{u}_c$ and $\delta\boldsymbol{\phi}$ are the variation of the position and the rotation of the reference point, respectively. The external load contribution is then:

$$\delta W_{\text{ext}} = \boldsymbol{F}\cdot\delta\boldsymbol{u}_c + \boldsymbol{M}\cdot\delta\boldsymbol{\phi} \tag{4}$$

Rigid bodies can have arbitrary shapes in Abaqus [36], and external faces may be discretised into several surface patches, so a rigorous evaluation of contact geometric interface and forces with other parts of the FE model may be performed.

2.2 Mechanical behaviour of contact joints

As the mechanical behaviour of contact joints is very complex, various rough surface contact models have been presented, e.g. the Hertz contact solution, the statistical contact model of rough surface, and the contact stiffness criterion, among others. In these cases, elastic-plastic contact between rough surfaces under normal and tangential loading is usually considered. Abaqus uses the constraint enforcement algorithm, which searches for node-into-face and edge-into-edge penetrations in the current configuration using the penalty contact method at each time increment [39]. In the mechanical behaviour of the contact, one of the main advantages of the penalty contact method is that it can mitigate over-constraint problems and reduce the number of iterations required by the analysis. If the contact is more discretised, the results are more accurate.

In the penalty contact method, the increase in normal force could be obtained linearly as follows:

$$\Delta F_n = K_n\,\Delta u_n\,A_c \tag{5}$$

where incrementΔu_n is the relative displacement between two bodies in contact (penetration between blocks), K_n is the normal contact stiffness or spring stiffness, and A_c is the contact area (Figure 3).

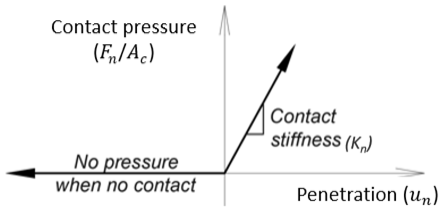

Figure 3. Non-linear penalty contact method – Normal stiffness.

In the case of the tangential behaviour, the increase in shear force could be obtained linearly as follows:

$$\Delta F_t = K_t \, \Delta u_t \, A_c \tag{6}$$

where Δu_t is the relative displacement between two bodies in tangential contact, and K_t is the tangential contact stiffness (shear stiffness). The maximum shear force is obtained from the Coulomb concept, i.e. slip occurs when the maximum possible frictional stress is reached (τ_{crit}):

$$F_{t\,crit} = \tau_{\text{crit}} \, Ac = F_n \tan\varphi = F_n \, \mu \tag{7}$$

where φ is the contact friction angle. In this case $\mu = \tan\varphi$ is the coefficient of friction. Whenever this maximum shear force is reached in a contact, the blocks slide [40, 41] (Figure 4).

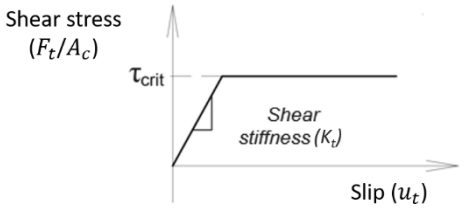

Figure 4. Coulomb friction model.

Figure 5 shows the behaviour of two blocks, A and B, subjected to gravity only and placed on an infinitely rigid inclined platform. Figure 5a shows the initial instant when gravity has not yet acted on the blocks. Figure 5b shows the moment when gravity is applied, generating a normal force (F_n). Due to the normal stiffness assumed (K_n), block B slightly gets in block A for a displacement u_n. Since the blocks are inclined, block B tries to slide away from block A due to its weight, and the tangential force (F_t) appears. Due to the tangential stiffness used (K_t), block B slides away from block A for a displacement u_t. If the tangential force reaches the $F_{t\,crit}$ in Equation 7, block B starts to slide. To ensure that u_n and u_t are very small and do not significantly affect the results, K_n and K_t must be very large. However, the computational time will increase drastically if these properties are too large. Although the blocks are individual rigid bodies, internally, they are divided into a set of elements kinematically linked to the block's rigid body degrees of freedom. This division enables, among other features, a detailed and adaptative computation of the contact forces when the interface area is modified according to the movement of the blocks.

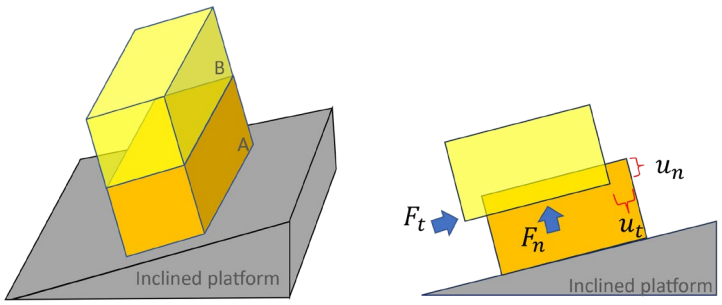

(a) (b)

Figure 5. Normal and tangential force between two blocks (a) Before gravity applied, (b) After gravity applied.

Finally, adding damping in the contact allows the dissipation of energy and the achievement of the equilibrium, reducing the computational time. In Abaqus, a damping force opposite to the motion is generated in the contact as follows:

$$F_d = \mu_0 \, A_c \, v_{rel} \tag{8}$$

where μ_0 is the damping coefficient, A_c is the contact area between the blocks, and v_{rel} is the relative velocity between the contact blocks. This incorporated damping force alleviates instabilities, oscillations, and noise, which are potential consequences of rapid fluctuations in contact forces or contact conditions.

3. Preliminary evaluation

Four rigid bodies and a validation model were analysed using 8 AMD RYZEN 7 5800H CPU @ 3.20 GHz processors from a server with 16 GB of shared RAM and a Windows 11 operating system. The first analysis consists of evaluating two blocks placed one on top of the other to verify the mechanical behaviour of the contact, and the second model represents an experimental test performed on a dry-stone wall.

3.1 Analysis of four rigid bodies

Figure 6 shows the behaviour of four rigid blocks subjected to the action of gravity for 2 s in Abaqus/Explicit. A time increment $\Delta t = 1 \times 10^{-4}$ s was used for this case and all the following ones. A smaller time increment could be used, but this would increase the computation time of the subsequent evaluations. The two bottom blocks (blocks 3 and 4) have negligible mass and are restrained to movement and rotation. Each block is discretised into C3D8R hexahedra. Each block is discretised into auxiliary C3D8R hexahedra. For the analysis of the dynamics of rigid bodies, Abaqus considers 6 DOF for each rigid block to represent arbitrary geometries and associated inertia properties of irregular blocks and better compute the contact forces among the blocks. These rigid blocks are divided into an arbitrary set of sub-elements, defined as C3D8R. However, these auxiliary elements do not contribute additional DOFs and are kinematically linked to the rigid body 6 DOF. The blocks are 0.220 × 0.105 × 0.050 m^3, with 2200 kg/m^3 density. Therefore, each block weighs 24.93 N. The values of stiffnesses are K_n equal to 1.96×10^7 N/m^3, and K_t equal to 0.82×10^7 N/m^3, while a friction angle of $\varphi = 38°$ and a damping coefficient $\mu_0 = 0.08$ were considered. The two upper blocks penetrate the lower blocks due to their weight and normal stiffness (Figure 6b). In this case, there are two normal acting forces between the three blocks because there are non-matching element faces: $F_{n\,1-3}$ (Blocks 1 and 3) and $F_{n\,1-4}$ (Blocks 1 and 4). On the other hand, if we evaluate only the joint between blocks 1 and 2, and replace the data in Equation 5, considering Δu_n as the relative displacement through which block 1 penetrates block 2, we obtain the following:

$$F_n = K_n \, \Delta u_n \, A_c \Longrightarrow \Delta u_n = 0.55 \times 10^{-4} \text{ m}$$

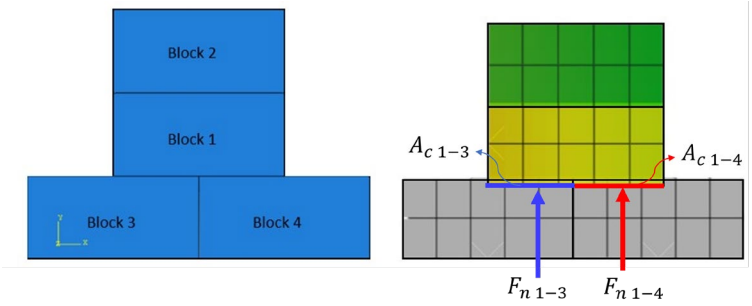

(a) (b)

Figure 6. Behaviour of four blocks under the action of gravity as modelled in Abaqus. (a) Before applying gravity, and (b) after.

Figure 7 shows the relative displacement between blocks 1 and 2, which is 0.55×10^{-4} m, and it is shown after 0.3 s. Note that there are some spurious oscillations before 0.3 s, and this effect happens because this is a non-linear explicit analysis where convergence is not evaluated and only the result of the previous increment is used. This value equals the 0.55×10^{-4} m calculated analytically.

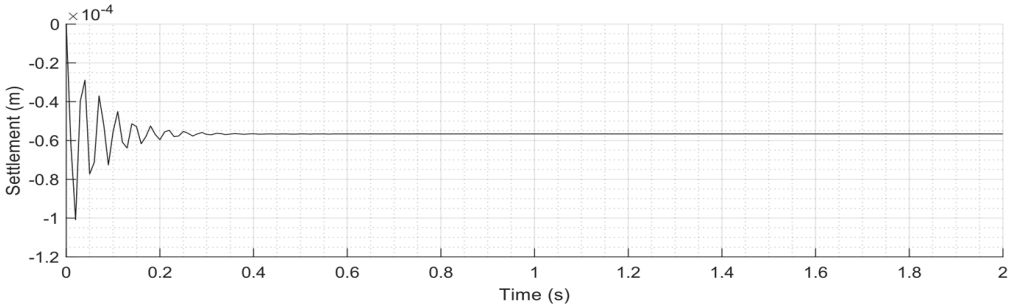

Figure 7. Relative displacement between blocks 1 and 2 under the action of gravity.

To verify Equation 7, block 3 was subjected to a 50 mm vertical settlement. The analysis started with 2 s for the effect of gravity and then 5 s for the effect of settlement, with a linear increment in both cases. Figure 8 shows the case in which block 3 suffers the 50 mm settlement. As shown, block 2 slides from block 1, and we can ensure that the maximum friction force has been exceeded in this joint. The maximum frictional force that can exist between blocks 1 and 2 is as follows:

$$F_{t\,crit} = F_n \tan\varphi = 24.93 \ \tan 38° = 19.47 \text{ N}$$

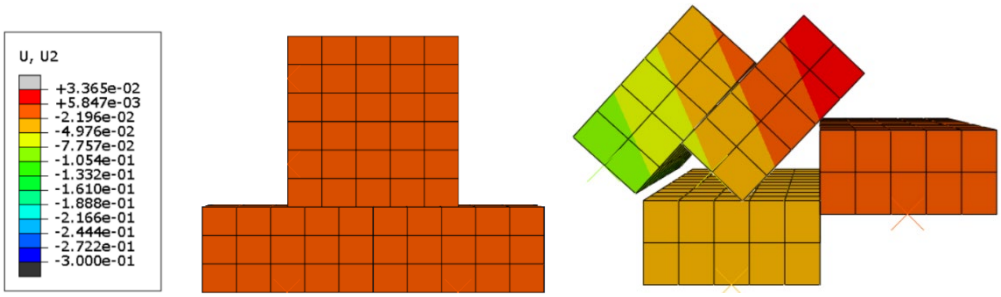

(a) (b)

Figure 8. Behaviour of four blocks under imposed settlement as modelled in Abaqus (units in m) (a) Before the settlement application and (b) after.

The computational time for this analysis was 1 min. Figure 9 shows the relationship between tangential force (N) and time (s). Note that the tangential force is null up to the application of gravity at 2 s. Then, the tangential force increases until 4.79 s, where block 2 starts to slide from block 1 since it reaches the maximum frictional force of 19.47 N. Figure 9 also shows how these blocks behave at different times. For this analysis, it was decided to use a time increment $\Delta t = 1 \times 10^{-4}$ s for the investigation.

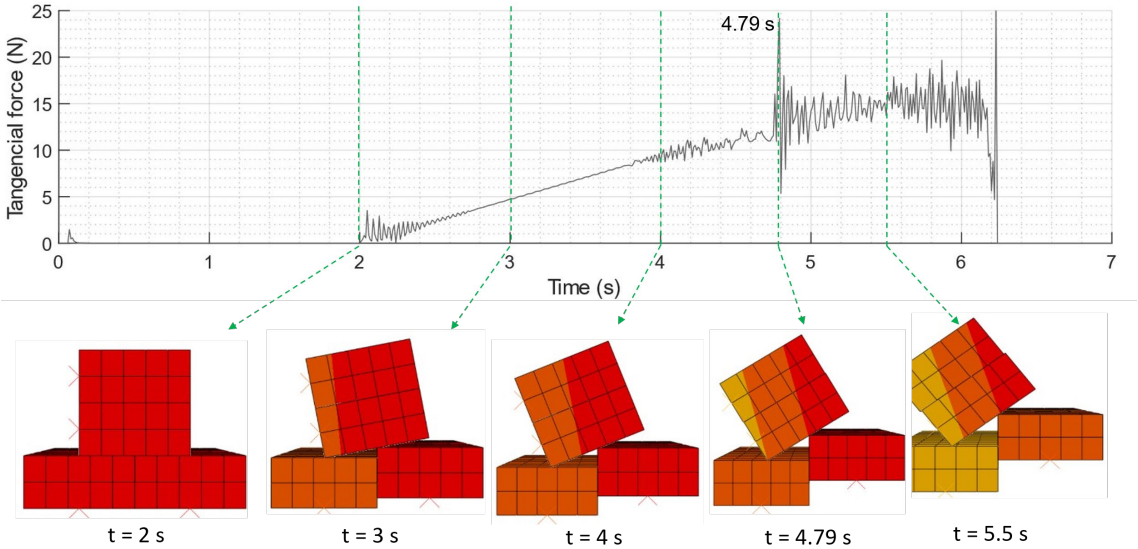

Figure 9. Tangential force generated in the contact between the two upper blocks due to settlement of one of the blocks.

3.2 Validation model. Simulation of experimental tests

The numerical methodology was validated by simulating the experimental tests by Santa-Cruz et al. [24], who built reduced-scale walls made of irregular stone blocks. Three walls were built with irregular stones (shale and limestone) and dry joints. Each wall was built with the same ashlars located in the same position. The stones had dimensions of approximately 100 × 50 × 150 mm^3. Each wall weighed about 1371 N, with a length of 1500 mm and a height of 375 mm. The walls were tested by applying an imposed base rotation through a timber structure. This structure contained a timber platform measuring 1600 × 600 × 40 mm^3, supported by two timber semicircles, and it was manually rotated by a lever and a pulley (Figure 10a). Note that the first row of blocks was constrained from moving or rotating as a boundary condition. Figure 10b

shows the dimensions of the tested walls. These three walls collapsed at an average angle of 14.33 degrees with a standard deviation of 0.76.

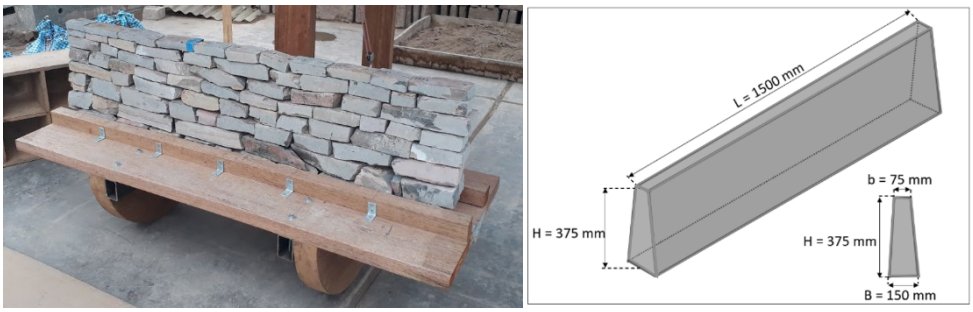

(a) (b)

Figure 10. Experimental tests executed by Santa-Cruz et al. [24]. (a) View of the wall, and (b) wall dimensions.

Abaqus/Explicit was used for the numerical modelling. The geometry of the blocks was defined by photographs taken from the front of the walls. The front face of the wall was drawn in AutoCAD, and each block was extruded as desired to create the 3D model made of blocks. Then, the 3D blocks were transferred to the Abaqus program in SAT format. As can be seen in Figure 10a, the wall did not have a constant cross-section, so the thickness of the wall was estimated from the dimensions of Figure 10b. The dimensions in Figure 11a are those used for the section of the model in Abaqus (Figure 11b). The ashlars were considered rigid bodies, and the mesh was composed of C3D8R hexahedra. In the analysis, it was assumed that each block has at least three hexahedra on each face.

The model included a rotating platform to simulate the timber platform used for the tests, which rotates around an axis of rotation. The wall and the rotating platform were placed on a discrete rigid platform that simulated the ground (Figure 11b). The first row of blocks was fixed in the rotating platform as boundary condition, according to that used by the authors in the experimental tests.

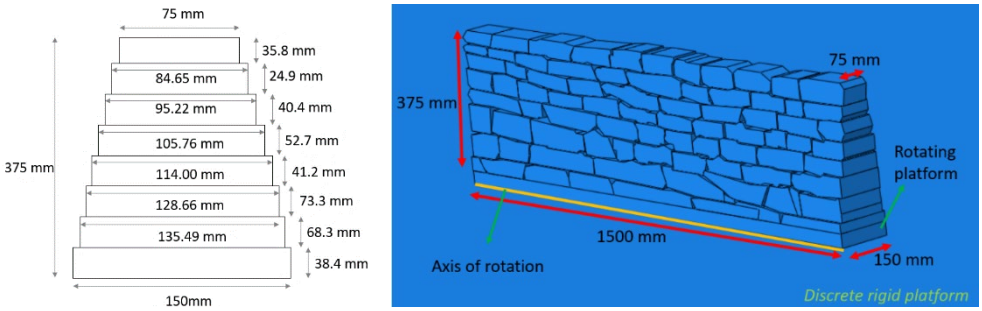

(a) (b)

Figure 11. Validation model: (a) Cross section of the wall, and (b) 3D view of the wall in Abaqus.

The model was calibrated through a parametric study of the contact properties. The block and contact properties obtained by Santa-Cruz et al. [24] were used to start the calibration. However, since these authors analysed the walls by DEM and with clump spheres, the properties of the model used for the present analysis are slightly different, as shown in Table 1. The density was adjusted to get the same weight as the real structure. A parameter $K_t = K_n/2$ and a similar Damping Coefficient as in [24] was considered. Finally, the Normal stiffness (K_n) and Coefficient of Friction (μ) were iteratively adjusted to achieve optimal agreement between the numerical and experimental wall displacements and collapse angles.

Table 1. Validation model. Assumed properties of the blocks and joints.

	Property	Symbol	DEM calibration (Santa-Cruz et al. [24])	FEM calibration (Present study)
Block	Density	ρ	2400 kg/m^3	2300 kg/m^3
Contact	Normal stiffness	K_n	5×10^7 N/m^3	2×10^8 N/m^3
	Tangential stiffness	K_t	2.5×10^7 N/m^3	1×10^8 N/m^3
	Coefficient of Friction	$\mu = \tan\varphi$	0.7	0.4
	Damping Coefficient	μ_0	0.8	0.8

The following steps were considered: i) the gravity was applied linearly and kept constant for up to 2 s; ii) the platform rotated at a higher speed of 1°/s until reaching 10° at 10 s; iii) the platform rotated at a slower rate of 0.2°/s up to collapse. The computational time for this analysis was 65 minutes. Figure 12 shows the behaviour of the wall at different time steps and degrees of inclination. In Figure 12a, the wall is at the initial instant. In Figure 12b, the wall, after 12 s, has already rotated 10°. In Figure 12c, the wall has an inclination of 13.6° and is still steady. In Figure 12d, at an inclination of 14.3°, various upper blocks detach from the structure. In Figure 12e, several blocks start to fall at an angle of 14.36°. Finally, Figure 12f shows what remains of the wall after overturning.

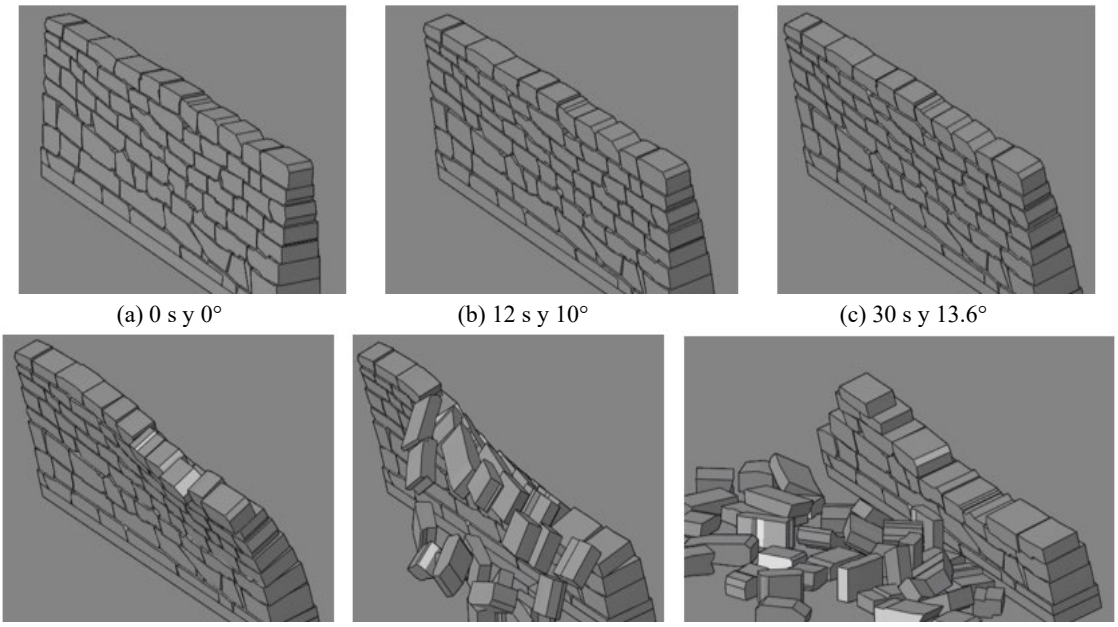

(a) 0 s y 0° (b) 12 s y 10° (c) 30 s y 13.6°

(d) 33.5 s y 14.3° e) 33.8 s y 14.36° (f) 36.3 s y 14.86°

Figure 12. Validation model. Configurations of the wall at different times and degrees of inclination.

Figure 13 shows the vertical reaction on the rotating platform at different times. As can be seen, the total weight of the model is 1373 N, which is very close to the real weight of the wall of 1371 N. The vertical reaction drops sharply at 33.5 s, corresponding to a rotation 14.3°. As shown in Figure 12d, it is precisely at this moment that the upper blocks begin to separate from the wall, and the model collapses. The angle associated with the model's collapse is the same as that experimentally reported. Figure 14 compares the collapse mechanisms of the experimental test and the numerical model. While the collapse mechanisms observed in the experimental and numerical models appear similar, the experimental model exhibits slightly larger displacements in the upper blocks. This discrepancy likely stems from the simplification employed in the numerical model, where the blocks were extruded, instead of replicating their intricate, irregular geometries in detail. Accurately capturing such complex features is a significant challenge in numerical simulations.

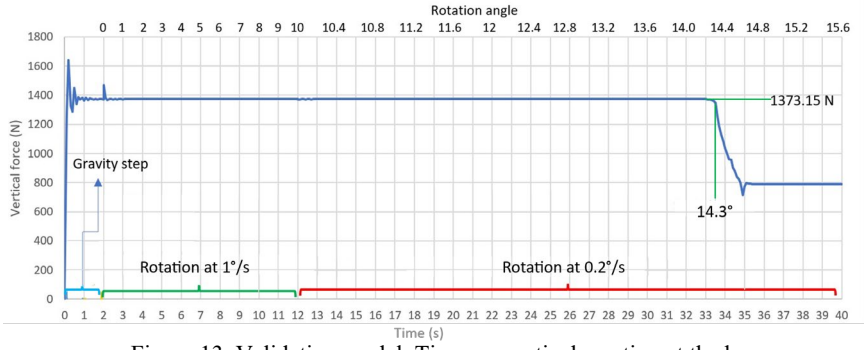

Figure 13. Validation model. Time vs. vertical reaction at the base.

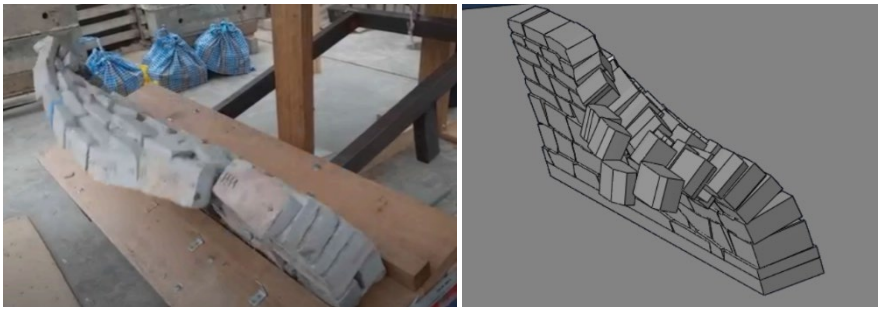

(a) (b)

Figure 14. Validation model. Collapse of the wall at 14.3º of inclination: (a) experiment, and (b) numerical model.

4. Case study: Sacsayhuaman archaeological site in Cusco, Peru

Sacsayhuaman is an archaeological site with an apparent ceremonial and military function, located in the hills of the extreme north of Cusco, Peru. The term means, in Quechua, “Place where the falcon is satisfied”. This archaeological site was built by the Inca culture, and its most notable feature is the presence of three continuous parallel walls with serrated lines distributed on stepped platforms [42] (Figure 15). The rocks used to build these structures were made of limestone [43]. The walls of Sacsayhuaman were never completed, and they were still under construction when the Spanish arrived [44].

Figure 15. Aerial view of Sacsayhuaman archaeological site.

Each wall is composed of large carved stones placed on top of the other with either irregular or coursed ashlar patterns. The number of stone leaves in these structures, acting as retaining walls, is likely variable. Figure 16 shows the three main typologies found in the archaeological complex of Sacsayhuaman. Most retaining walls are made of medium to large stones (size from 0.2 to 8 m), dry jointed, and with irregular patterns (typology 1). In addition, there are single-leaf walls with medium-size dry coursed ashlars (size from 0.2 to 0.8 m) (typology 2). Finally, there are walls with medium-sized carved stone (0.2 to 0.8 m), with two leaves of irregular pattern and intermediate infill (typology 3).

(a) (b) (c)

Figure 16. Taxonomy of the walls of the Sacsayhuaman complex: (a) typology 1 with an irregular pattern, (b) typology 2 with coursed ashlars, and (c) typology 3 with two leaves of irregular pattern and intermediate infill.

A large part of the wall of the third platform was damaged in 2009, and a portion collapsed out of its plane on January 14, 2010 (Figure 17). The leading cause was assumed to be the lateral soil pressure derived from

excessive runoff due to precipitation and seismic motion at the site [45]. Alva et al. (2016) evaluated the soil's dynamic response in the archaeological site of Sacsayhuaman by using microtremors, and they obtained values between 1.75 and 2.86 Hz and an acceleration amplification of 1.56 compared to the bedrock layer [46]. Note that this amplification depends significantly on the soil characteristics [47], so different archaeological sites in Cusco may have different amplification.

The walls in Sacsayhuaman are currently in good conservation condition. However, during the inspection, slight settlements were observed in many locations of the archaeological complex.

Figure 17. Collapsed section of a wall in Sacsayhuaman in 2010 [48].

In addition, the Cusco region is in an area of active cortical faults, generally oriented NW-SE with a normal N-S motion. The main faults are Coricocha, Tambomachay, Pachatusan, and Cusco (Figure 18). The extension of the faults appears to be generally due to gravity and buoyancy forces exerted by the thick crust uplifted above its isostatic equilibrium depth in the Cordillera. It is estimated that the maximum moment magnitude of an earthquake at this site is Mw 7.2 [6]. However, history showed that even smaller earthquake motions could have important consequences, such as the telluric motions that occurred in 1650, 1744, and 1950. Furthermore, according to colonial chronicles, it is believed that an earthquake of significant magnitude could damage various Inca structures between 1438 and 1463 (such as the cases in Figure 2). However, this is just a hypothesis of these structural damages [49]. Unfortunately, these earthquakes were not recorded, so how the terrain behaved during those years is unknown.

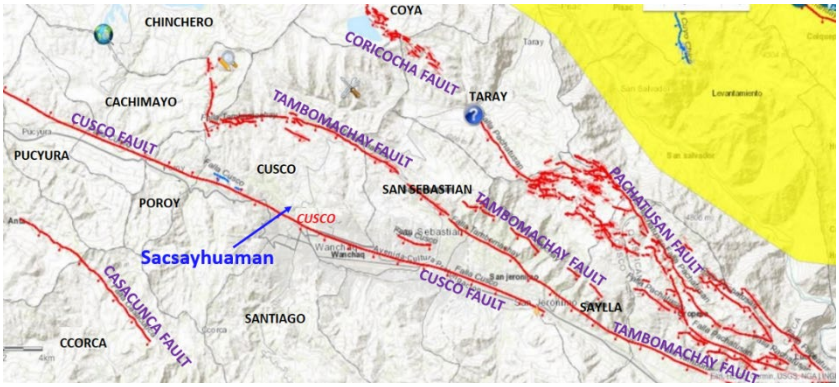

Figure 18. Active faults of Coricocha, Pachatusan, Tambomachay, and Cusco [50].

4.1 Numerical modelling of a wall section in the Sacsayhuaman site

Figure 19a shows the Sacsayhuaman walls of the different platforms, Figure 19b shows the section of the Sacsayhuaman wall considered in this study (red circle in Figure 19a), and Figure 19c shows this section modelled in Abaqus with the 40 numbered ashlars, together with the four control points assumed at the top of the structure. Points A, B, C and D correspond to blocks 35, 38, 39, and 40, respectively. The mesh of the ashlars was made of C3D8R hexahedra, and each face of each ashlar has at least three hexahedra (as in the validation model). It was also considered a base platform on which the wall rests, with negligible weight and infinite rigidity. The wall section has a length of 8.64 m, a height of 4 m, and an approximate thickness of the external layer of 0.8 m. The wall blocks were drawn in AutoCAD according to the geometry of the front face of the wall (Figure 19b), and each block was considered to have a thickness of 0.8 m. Finally, this drawing was exported to the Abaqus/Explicit program. As the internal geometry of the layers of these

walls is uncertain to date, only the external layer of the wall was evaluated in this study. Note that the thickness of 0.8 m was assumed because many Inca walls have this thickness [4], but the exact thickness of Sacsayhuaman's walls is still unknown.

(a)

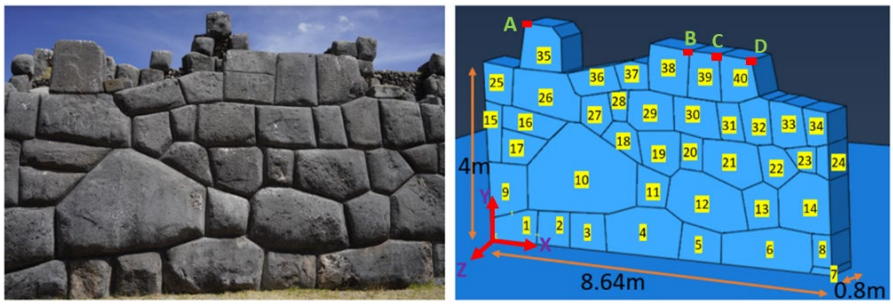

(b) (c)

Figure 19. Sacsayhuaman site: (a) general view, (b) section of the evaluated wall, and (c) model of the evaluated section in Abaqus.

The same physical and mechanical properties of the validation models of Section 3 were used for the wall section of Sacsayhuaman (Table 1). As for the boundary conditions, the rigid platform could not move or rotate during the application of gravity. After the start of the dynamic analysis, the platform can only move in the axis perpendicular to the wall. Since the wall is supported directly on the rigid platform (Figure 19a), it is considered that each block in contact with the rigid platform is fixed (from blocks 1 to 7 in Figure 19c). In addition, any block at the vertical sides of the wall, which is not in contact with the platform, can only move vertically and in the axis perpendicular to the wall, as well as rotate out of the plane of the wall (blocks 9, 15, 25, 8, 14, 24, 34).

4.2 Vibration-based approach. Evaluation of the fundamental frequencies of the wall using white noise

Vibration-based approach is performed by placing a specimen on the ground and applying controlled external vibrations of very low amplitude (e.g. white noise or sinusoidal motions). The low-amplitude excitation enables linear dynamic analysis, which is crucial as the highly non-linear behaviour of dry joints at larger amplitudes renders linear dynamics unsuitable for extracting accurate modal properties [32, 51]. Many authors choose this approach when the modal analysis is complex or impossible [52, 53]. To know the predominant frequencies of the wall in its perpendicular axis, a white noise with a maximum displacement of less than 1 mm and a sampling frequency of 1000 Hz was applied at the base of the wall (Figure 20a). Figure 20b shows the Fourier spectrum of this signal, and the predominant frequencies range from 0 to 20 Hz.

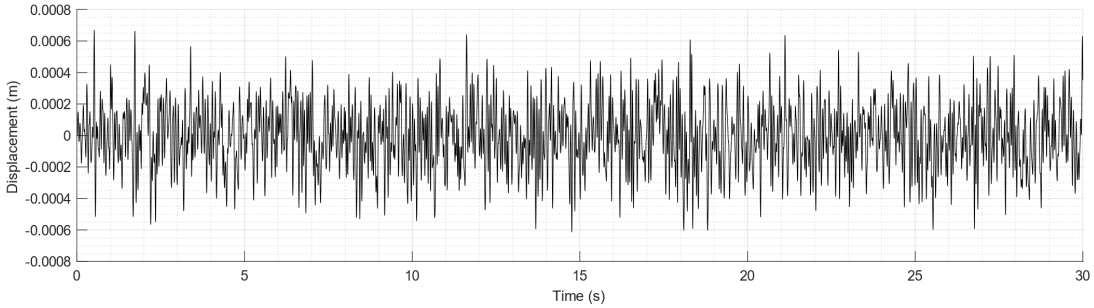

(a)

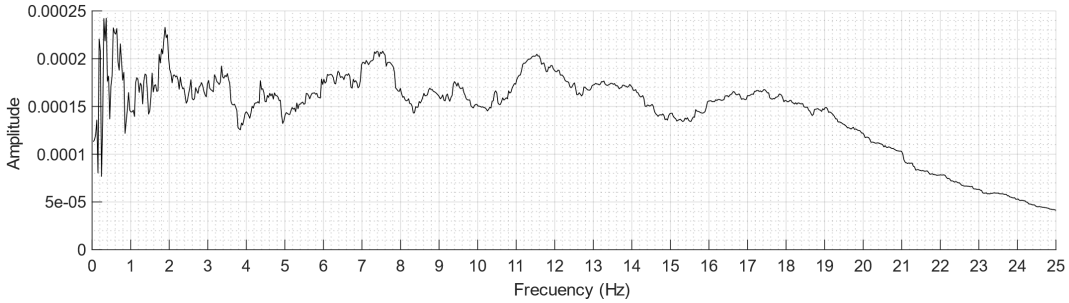

(b)

Figure 20. White noise: (a) signal and (b) Fourier spectrum.

The analysis was performed using Dynamic-Explicit analysis, with a time step of $\Delta t = 1 \times 10^{-4}$ s. For this analysis, the first step considered the application of gravity, with a linear increment up to 1 s that remained constant until 2 s. A second step, apply the white noise for 30 s, with the platform moving perpendicular to the plane of the wall.

The computational time for this analysis was 6 hours and 48 minutes, using 8 AMD RYZEN 7 5800H CPU @ 3.20 GHz processors on a server with 16 GB of shared RAM and a Windows 11 operating system.

After the analysis, the time history of the out-of-plane displacement was evaluated at the base and control points A, B, C, and D on the wall. The Fourier spectrum of each record was then obtained to determine the predominant frequencies of the wall (Figure 21). As can be seen, in the four control points evaluated, the peak frequencies are similar, and they are 0.488, 0.976, 1.464, 4.638, 9.520, 10.254, 13.428 and 14.893 Hz.

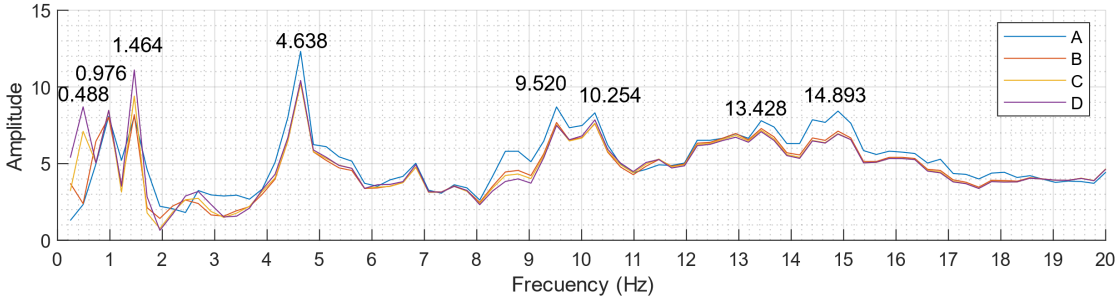

Figure 21. Fourier spectrum corresponding to control points A, B, C and D.

4.3 Vibration-based approach. Evaluation of the wall section for different signals

Another vibration-based technique was considered since various predominant frequencies were obtained in the previous evaluation. The structure was subjected to sinusoidal out-of-plane motions at the base. The motion of the ground is in the time domain:

$$Displacement\ (t) = 0.5/(\omega_n^2)\ \sin(\omega_n \times t) \tag{9}$$

where ω_n is the angular frequency. The double derivative of Equation 9 provides the acceleration, i.e. $0.5\ \sin(\omega_n \times t)$. The system's frequency is:

$$Frequency = \omega_n/(2\pi) \quad (10)$$

Note that a displacement signal was used to impose the sinusoidal motion because this assumption forced the system to have a magnitude equal to zero in displacement, velocity, and acceleration at the end of each cycle.

The system was subjected to various out-of-plane sinusoidal motions at the base, with frequencies ranging from 0.1 to 20 Hz. In all these cases, the maximum acceleration was 0.5 m/s^2. For this analysis, the first step considered the application of gravity, with a linear increment up to 1 s that remained constant until 2 s. A second step applied the sinusoidal motion for 10 s, with the platform moving perpendicular to the plane of the wall accordingly.

Figure 22 shows the displacement behaviour of point A relative to the base at the different frequencies mentioned. In this analysis, the 0.1 Hz frequency was not considered since sudden movements were induced at the beginning of the motion. As shown in Figure 22, the frequencies that generate the most significant relative displacements are the sinusoidal motions with frequencies of 0.9 and 1 Hz, with the 0.9 Hz frequency producing the most significant relative displacements. This evaluation was also evaluated for points B, C and D, and the response of the maximum peaks of the relative motion was also found for frequencies of 0.9 and 1 Hz. The computational time for this analysis was 48 minutes for each frequency evaluated.

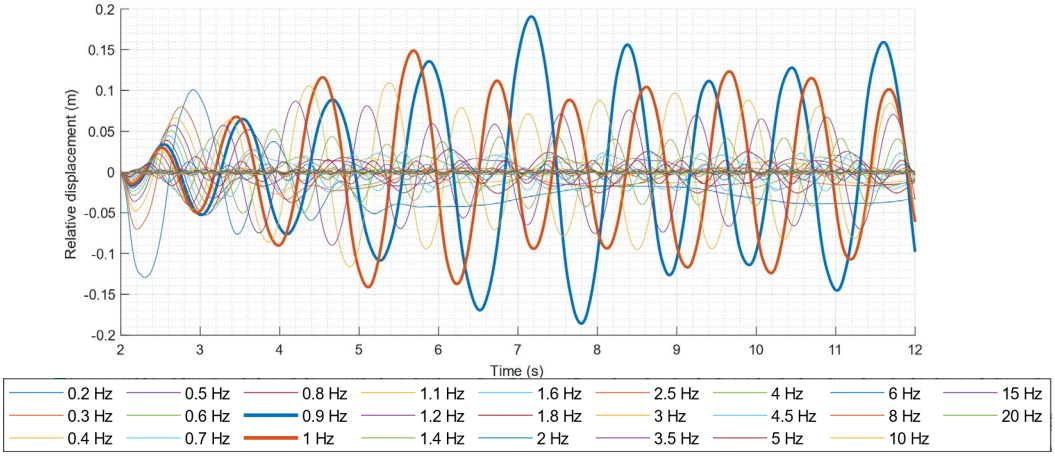

Figure 22. Relative displacement of point A for different sinusoidal motions.

The structure was also evaluated according to sinusoidal displacements with the frequencies obtained by the white noise analysis (Figure 21). Figure 23 shows the relative displacement of point A derived from sinusoidal motions with the frequencies obtained from the white noise. As can be seen, the sinusoidal displacement with a frequency of 0.976 Hz is the one that produces the most significant relative displacement of point A. The same occurs with the relative displacements of points B, C and D. For these reasons, we can conclude that the dominant out-of-plane frequency is approximately 0.976 Hz.

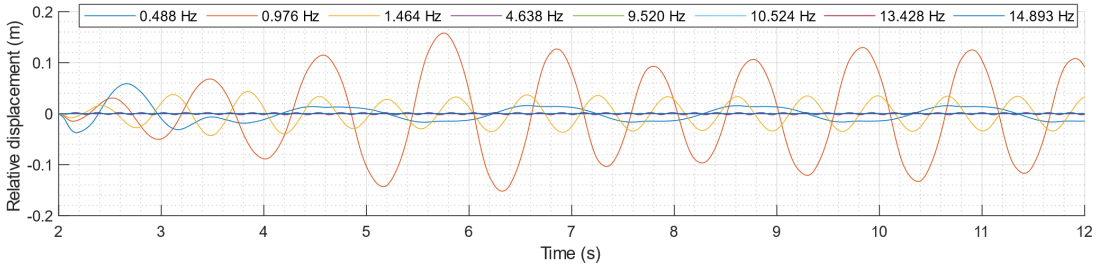

Figure 23. Relative displacement of point A for sinusoidal motions with predominant frequencies.

Based on the previous results, the behaviour of the structure was evaluated for a sinusoidal motion with a frequency of 0.976 Hz and with scaled Peak Ground Acceleration (PGA) at the base, ranging from 0.1g to

0.9g. Figure 24 shows the state of the structure after the sinusoidal motion of 10 seconds duration with a frequency of 0.976 Hz and different PGAs. When the PGA is 0.1g or 0.2g, permanent or residual displacements are seen in block 35. When PGA is 0.3g, permanent displacements are seen in blocks 35, 38, 39 and 40. When PGA is 0.4g, the collapse of blocks 35, 38, 39 and 40 is seen, and so on, until the wall has wholly collapsed for a PGA of 0.9g.

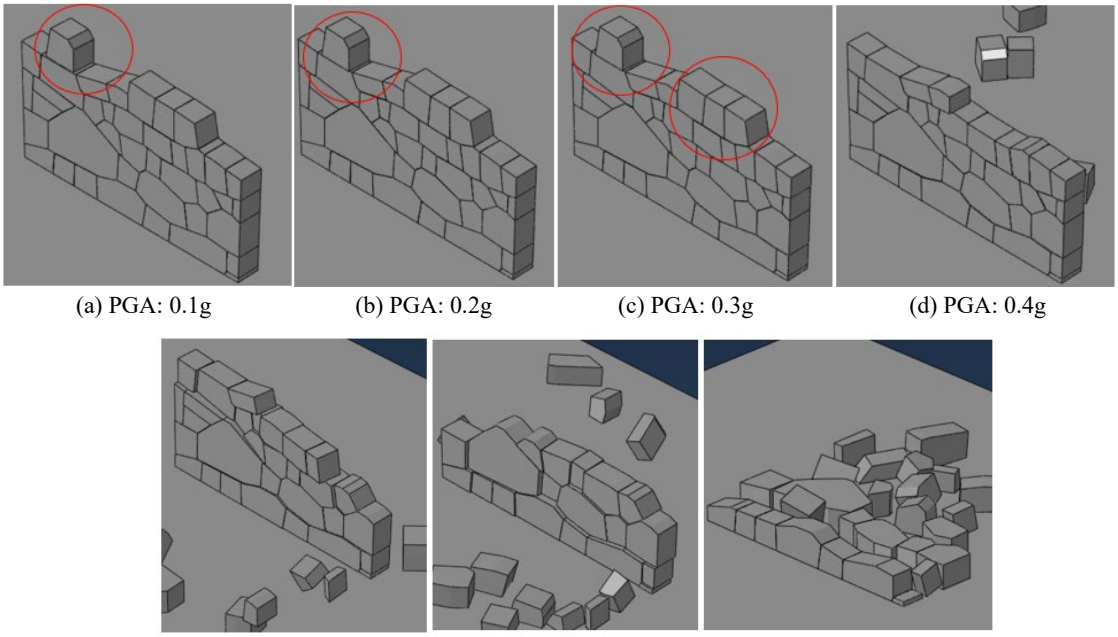

(a) PGA: 0.1g (b) PGA: 0.2g (c) PGA: 0.3g (d) PGA: 0.4g

(e) PGA: 0.6g (f) PGA: 0.8g (g) PGA: 0.9g

Figure 24. Final state of the structure after a sinusoidal motion at the base with a frequency of 0.976 Hz for different scaled PGA.

5. Evaluation of the wall section for different earthquakes

The behaviour of the structure was evaluated for three seismic records, i.e., two originated from the tectonic faults of Cusco, and the other was representative of the largest earthquake recorded in Peru in the last century (Ancash earthquake, 1970). Note that the last one was not generated by an intraplate fault but by the subduction process between plates along the coast of Peru [54]. The seismic records and their details are shown in Table 2.

Table 2. Details of the seismic records evaluated.

Earthquake	Date	Magnitude	PGA	Depth (km)	Seismic station	Station built on
Paruro, Cusco [55]	September 27, 2014	5.1 Ml	0.01g	6	Tambomachay, Cusco	Rock
Cusco city [56]	February 18, 2023	3.8	0.054g	14	Wanchaq, Cusco	Clayey gravel
Ancash [57]	May 31, 1970	6.6 Mb	0.1g	1	Parque de la Reserva, Lima	Alluvial rock

For this analysis, a first step considered the application of gravity, with a linear increment up to 1 s that remained constant until 2 s. A second step applied the dynamic action, with the platform moving according to the considered seismic record.

5.1 Evaluation of the structural behaviour under the seismic record of Paruro, Cusco, 2014

Figure 25a shows the seismic record of the Paruro earthquake (only the first 60 s of the seismic record were used), and Figure 25b shows the Fourier spectrum of the seismic signal. As can be seen, the predominant frequencies of the record are between 0.46 Hz and about 1 Hz. In this case, the dominant frequency of the wall of 0.976 Hz is within the range of predominant frequencies of the seismic record.

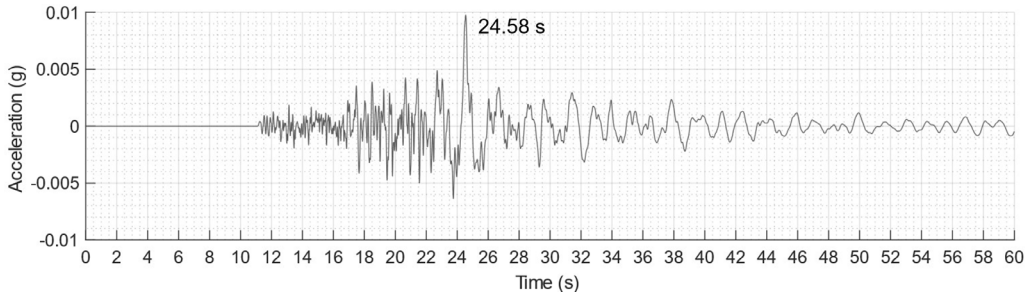

(a)

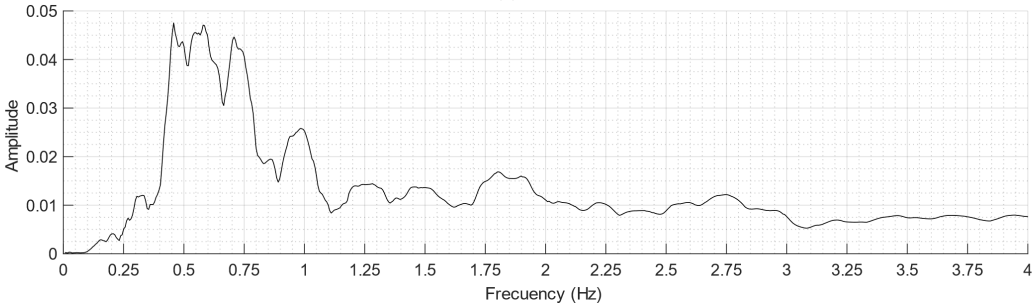

(b)

Figure 25. Paruro earthquake, Cusco (Seismic station: Tambomachay): (a) seismic record, and (b) Fourier spectrum.

The structural behaviour of this construction was evaluated by scaling the earthquakes for different PGAs. This process was carried out to identify specific failure mechanisms and the most vulnerable/critical areas [27]. The computational time for each analysis was 1 hour. Figure 26 shows the state of the structure after the seismic recording with various PGAs. At first glance, the structure does not suffer any damage for a seismic record scaled to a PGA of 0.3g. However, for a PGA of 0.4g, the system collapses abruptly due to overturning. As shown in Figure 25a, there is a peak motion at 24.58 s in the seismic record, which coincides with the collapse due to the overturning of the structure.

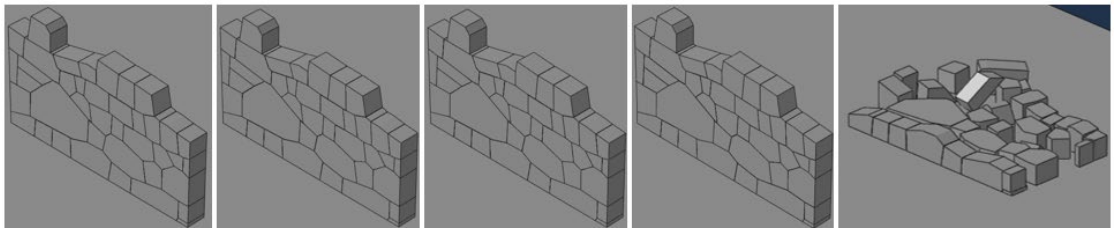

(a) PGA: 0.01g (b) PGA: 0.1g (c) PGA: 0.2g (d) PGA: 0.3g (e) PGA: 0.4g

Figure 26. States of the structure after the Paruro seismic record scaled for different PGAs.

Figure 27 shows the behaviour of the relative displacement of point A due to different PGAs. Massive motions are generated at 24.58 s, given by the peak motion in the seismic record. This sudden motion is the cause of the collapse of the structure when the seismic record is scaled for PGA of 0.4g. It is also seen that for a PGA of 0.3g, the maximum relative displacement is 0.9 m.

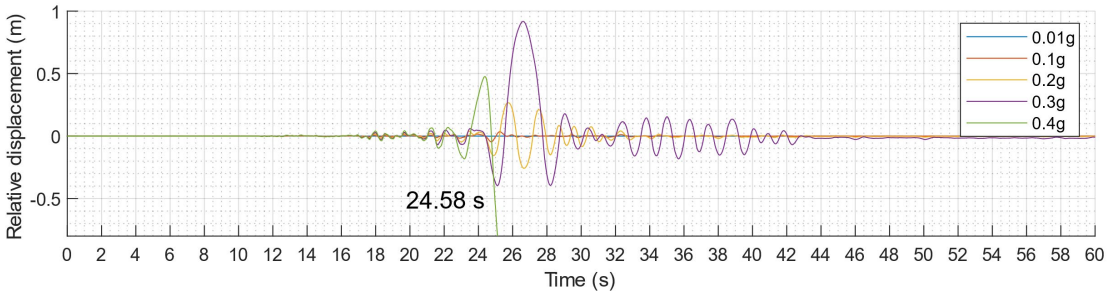

Figure 27. Relative displacement of point A due to the Paruro seismic record.

5.2 Evaluation of the structural behaviour under the seismic record of Cusco, February 18, 2023

Figure 28a shows the seismic record of the earthquake in Cusco on February 18, 2023. Figure 28b shows the Fourier spectrum of the seismic signal. As can be seen, the predominant frequencies range from 1.5 Hz to higher values. In this case, the dominant frequency of the wall of 0.976 Hz is not among the predominant frequencies of the seismic record. In addition, the arrival of the longitudinal waves (at 3.97 s) and of the transverse waves (at 5.36 s) can be seen in the seismic signal.

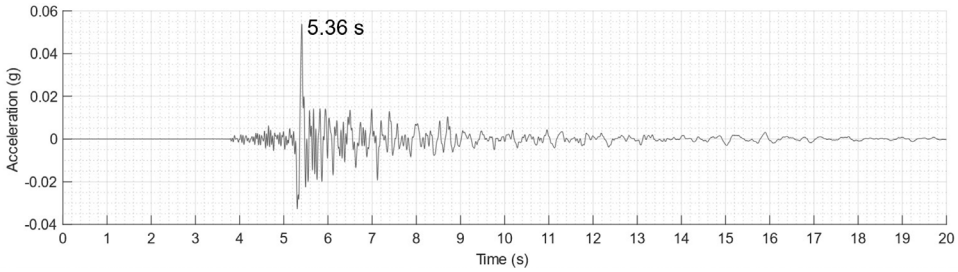

(a)

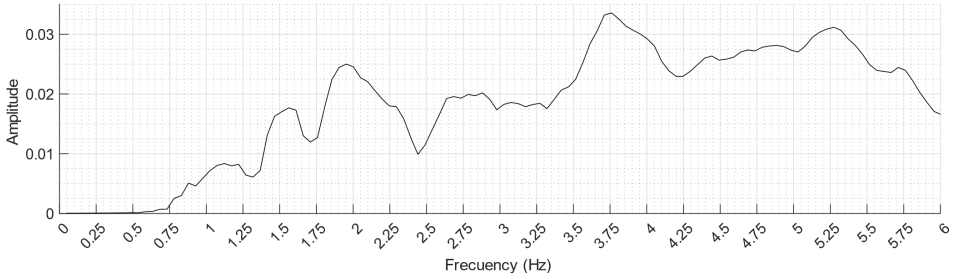

(b)

Figure 28. Cusco earthquake of February 18, 2023 (Seismic Station: Wanchaq): (a) seismic record, and (b) Fourier spectrum.

Since the PGA of this earthquake was 0.054g, the structural behaviour of this construction was evaluated by scaling this record to different PGAs. The computational time for each analysis was 37 minutes. Figure 29 shows the structure's state after applying seismic recording with different PGAs. Approximately up to a PGA of 0.4g, the structure does not suffer any noticeable damage, and only for a PGA of 0.5g relative displacements appear in different blocks. No block of the system collapses in seismic recordings with a high PGA of 1g and 2.5g. Despite these strong motions, the structure does not collapse. As mentioned above, as the seismic record of the Cusco earthquake of 2023 has very high predominant frequencies far from the dominant frequency of the wall, it does not directly affect the structure.

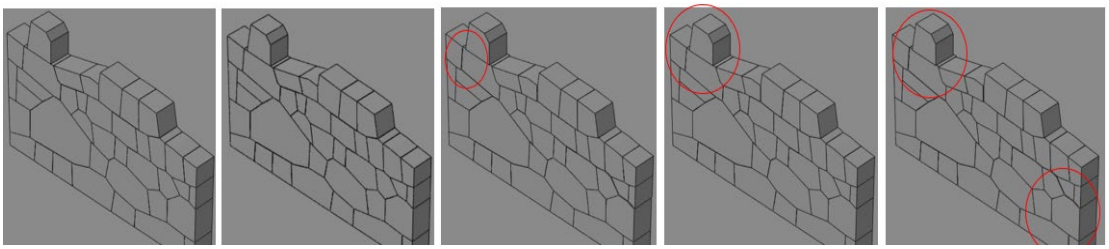

(a) PGA: 0.1g (b) PGA: 0.4g (c) PGA: 0.5g (d) PGA: 1g (e) PGA: 2.5g

Figure 29. States of the structure after the seismic recording of February 18, 2023, Cusco, scaled to different PGAs.

Figure 30 shows the evolution of the relative displacement of point A under the seismic records scaled to PGAs ranging from 0.1g to 0.5g. Only these PGAs were evaluated because the relative displacements were very high for larger PGAs, and according to a seismic hazard study in Peru, a PGA of 0.5g is the approximate maximum PGA that could occur in 50 years, with a 10% probability of being exceeded [58]. As seen in Figure 30, large motions are generated at 5.36 s, which coincides with the peak of the seismic record. It can also be seen that the relative displacements at point A are not as large as in the previous case, where they reached 0.90 m with a PGA of 0.3g, and in this case, with a PGA of 0.5g, they reach only 0.14 m.

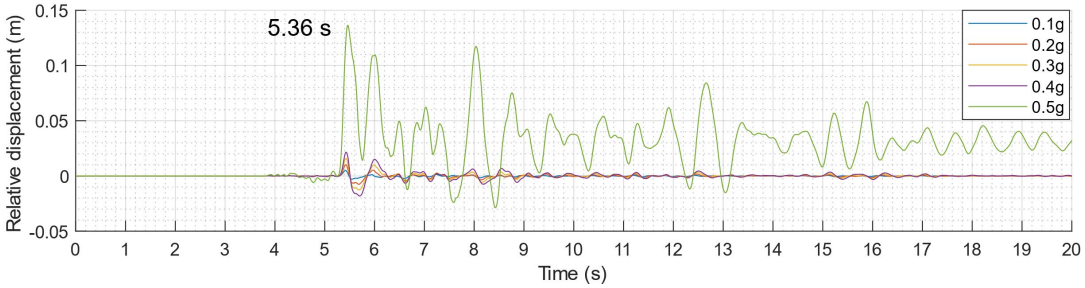

Figure 30. Relative displacement of point A due to the Cusco 2023 seismic record.

5.3 Evaluation of the structural behaviour under the seismic record of Ancash on May 31, 1970

Figure 31a shows the seismic record of the Ancash earthquake. Figure 31b shows the Fourier spectrum of this signal. As shown in Figure 31b, the predominant frequencies of the record are between approximately 1.3 and 13 Hz, which are higher than the dominant frequency of 0.976 Hz of the wall. Although this earthquake occurred in a subduction zone far from the Sacsayhuaman site, it was used in this evaluation because it caused one of the greatest natural destructions in Peru. This earthquake affected about 83000 km^2 on the surface, causing the death of 70000 inhabitants and causing damage to more than 16000 buildings, around 80% of the structures in the area [59]. This earthquake caused a large avalanche that buried the town of Yungay [60].

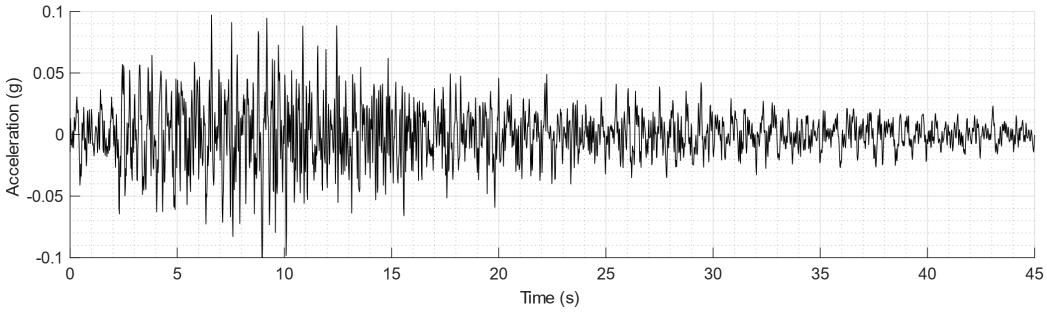

(a)

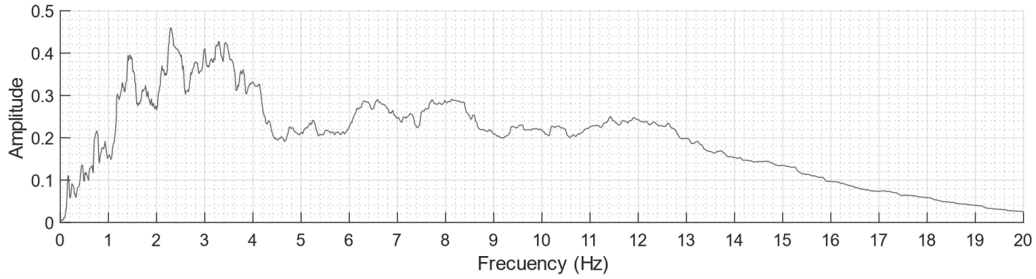

(b)

Figure 31. Ancash 1970 earthquake (Seismic Station: Parque de la Reserva): (a) seismic record, and (b) Fourier spectrum.

Figure 32 shows the state of the structure after the analyses with seismic recordings scaled to different PGAs. The computational time for each analysis was 63 minutes. The system does not suffer any noticeable damage up to a PGA of 0.4g, while for a PGA of 0.5g, perceptible relative displacements appear (very similar to the previous case). It can also be seen that the structure suffers a partial collapse for a PGA of 2g and a complete collapse at 2.5g. As mentioned, this earthquake had high predominant frequencies, so they did not affect the structure.

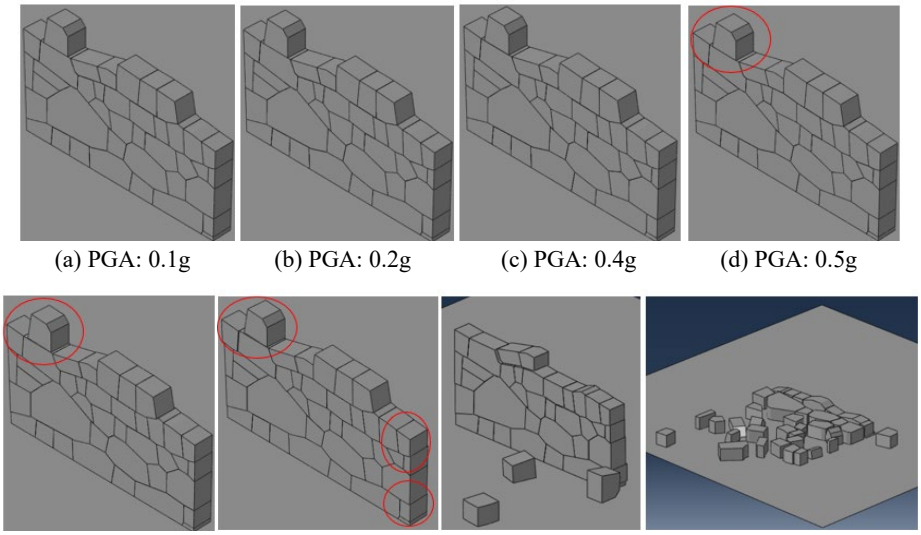

(a) PGA: 0.1g (b) PGA: 0.2g (c) PGA: 0.4g (d) PGA: 0.5g

(e) PGA: 1g (f) PGA: 1.5g (g) PGA: 2g (h) PGA: 2.5g

Figure 32. States of the structure after the Ancash 1970 earthquake for different PGAs.

Figure 33 shows the evolution of the relative displacement of point A during the seismic record, with a PGA ranging from 0.1g to 0.5g. The relative displacements are small, very different from those derived from the Paruro 2014 seismic record study.

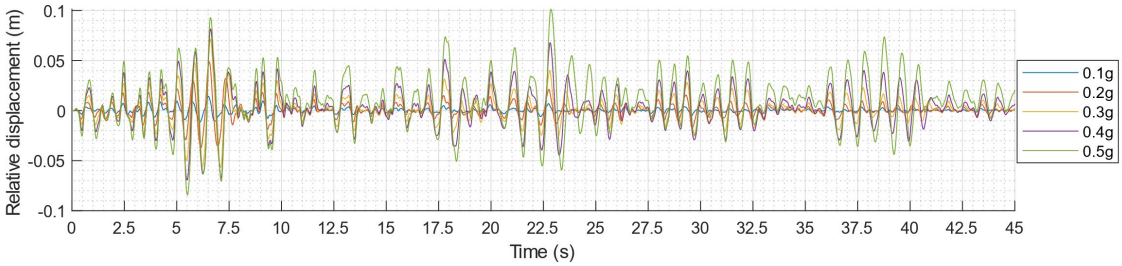

Figure 33. Relative displacement of point A due to the Ancash 1970 seismic record.

5.4 Residual displacements of the structure at the end of each seismic record

Table 3 shows the block(s) that suffered the largest remaining displacements at the end of each analysis. These displacements are relative to the base. The blocks that sustained the most significant displacements were generally those in the upper part of the wall, i.e. blocks 35, 38, 39 and 40 (points A, B, C and D, respectively). The residual displacements seem to be of small magnitude for PGAs less than 0.3g. However, it is essential to remember the importance of preventing these structures from having important residual deformations after a seismic event. As can be seen, if the earthquakes had a PGA of 0.1g, the residual displacement would be minimal, less than 1 mm. With a PGA of 0.2g, the structure would have a residual displacement of almost 3 mm, which could be very noticeable in these constructions. The damage could be severe with a PGA of 0.3g or higher. As already mentioned, an earthquake with Mw 7.2 could be generated in Cusco and, according to a geophysical study, if the Tambomachay fault caused an earthquake of Mw 7.01, a PGA greater than 0.45g would be generated in the districts of Poroy, Santiago, Cusco, Wanchaq, San Sebastián and San Gerónimo, which could cause severe damage to Inca structures [61].

Table 3. Maximum remaining displacement after each event (mm).

	2014 earthquake, Paruro, Cusco		2023 earthquake, Cusco		1970 earthquake, Ancash	
PGA	Maximum residual displacement (mm)	Referred stone	Maximum residual displacement (mm)	Referred stone	Maximum residual displacement (mm)	Referred stone
0.1g	0.5	35	0.3	38, 39, 40	0.6	39, 40
0.2g	2.9	35	0.3	35	1.8	35
0.3g	12.0	38, 39, 40	0.1	35	3.0	37
0.4g	collapse	all	0.1	35	7.3	35
0.5g	collapse	all	0.7	40	21.4	35
1g	collapse	all	20.0	35	112.5	39, 40
1.5g	collapse	all	31.8	35	129.9	25
2g	collapse	all	32.4	35, 36	collapse	35, 38, 39, 40
2.5g	collapse	all	32.1	35, 36, 37	collapse	all

Figure 34 compares the out-of-plane relative displacement of point A (block 35) during the seismic records with a scaled PGA of 0.2g. As shown, the 2014 Paruro earthquake produced the largest relative displacements due to the proximity of the predominant frequency of the seismic record to that of the evaluated structure.

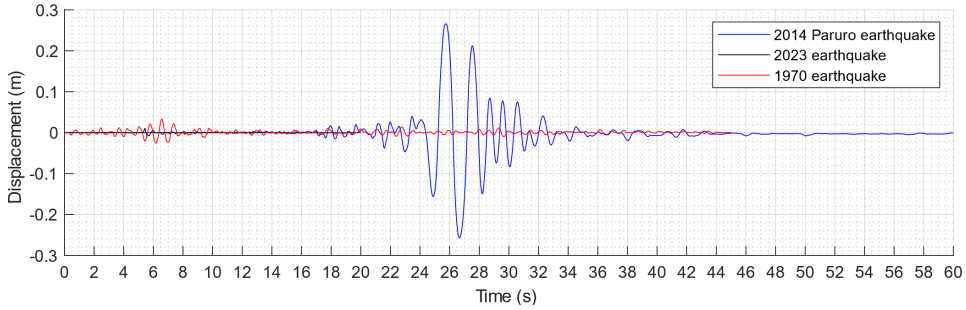

Figure 34. Relative displacement of point A due to the seismic records scaled to a PGA of 0.2g.

6. Conclusions

This research has addressed the challenge of evaluating the seismic response of irregular stone structures like Inca constructions. It has presented a novel numerical strategy based on the finite element method, combining the dynamics of rigid body and contact laws. A 3D model was created to analyse the behaviour under different peak ground accelerations related to various Peruvian earthquake scenarios. This approach effectively captures the dynamic behaviour, failure mechanisms, and relative displacements of the dry-jointed stones, providing valuable insights into the seismic vulnerability of these historical structures.

The overturning behaviour of the stone constructions in the dynamic regime is significantly influenced by their dominant frequency and the frequency content of the seismic record. The vibration-based approach is a helpful alternative to calculate the natural out-of-plane frequency of a dry-joint stone structure. This work has considered a wall section of Sacsayhuaman subjected to a white noise signal and then to a series of sinusoidal signals of different frequencies. After executing numerical analyses for different Peruvian earthquakes, the Paruro seismic record has been shown to cause significant damage to the structure since its natural frequency was within the frequency content of the seismic record. In the worst case, the Paruro earthquake scaled to a PGA of 0.4g might lead the structure to collapse. A PGA of 0.2g could also severely damage the structure, regardless of the frequency of the earthquake.

The conservation and maintenance of heritage buildings are crucial tasks because they help preserve a city's history and identity, as well as its artistic and architectural value. The city of Cusco is considered a World Cultural Heritage Site by UNESCO for its exceptional universal value as a masterpiece of human creative

genius. Unfortunately, these magnificent structures are near active cortical faults, which might generate strong earthquakes with a PGA greater than 0.45g and an acceleration amplification of 1.56 to the bedrock layer. For these reasons, it is essential to systematically evaluate all these historical monuments and propose appropriate interventions for their preservation. Numerical analyses can provide helpful information about the blocks of each stone structure that may suffer residual displacements or even collapse after a seismic event. Knowing the limitations of this work, further research should be addressed to evaluate the effects of soil pressure on single and multi-leave stone walls, also by performing experimental tests to better compute the mechanical contact properties. Finally, as it was demonstrated that the frequency content of the seismic input is crucial for the dynamic response of the stone walls, further analysis considering ground motion amplification due to site conditions may also be done.

7. Appendix

All the videos regarding the non-linear time-history analyses can be downloaded from:

8. Acknowledgements

The authors thank the support of the FAI-2021 funds of the Pontificia Universidad Católica del Perú (PUCP), the School of Graduates of the PUCP, the Universitat Politécnica de Catalunya, the Computational Mechanics Group of the Universidad Politécnica de Madrid, and the NextGeneration-EU program.

9. Bibliography

[1] Savalle, N., Blanc-Gonnet, J., Vincens, E., & Hans, S. Dynamic behaviour of dry-stone retaining walls: shaking table scaled-down tests. European Journal of Environmental and Civil Engineering, 26(10), 4527-4547, 2022. https://doi.org/10.1080/19648189.2020.1855477

[2] Gürbüz, M., & Kocaman, İ. Enhancing seismic resilience: A proposed reinforcement technique for historical minarets. Engineering Failure Analysis, 156, 107832, 2024. https://doi.org/10.1016/j.engfailanal.2023.107832

[3] Béarez, P., & Miranda, L. Análisis arqueo-ictiológico del sector residencial del sitio arqueológico de Caral-Supe, costa central del Perú. Arqueology and Society, (13), 10-11, 2000.

[4] Agurto, S. Construcción, arquitectura y planeamiento incas. Lima: CAPECO editorial, 119, 1987.

[5] Protzen, J. P. Inca quarrying and stonecutting. The Journal of the Society of Architectural Historians, 44(2), 161-182, 1985. https://doi.org/10.2307/990027

[6] Combey, A., Audin, L., Gandreau, D., Benavente, C., Rosell, L., & Marconato, L. Reassessing the seismic hazard in the Cusco area, Peru: New contribution coming from an archaeoseismological survey on Inca remains. Quaternary International, 634, 81-98, 2022. https://doi.org/10.1016/j.quaint.2022.07.003

[7] Rodríguez-Pascua, M. A., Benavente Escobar, C., Rosell Guevara, L., Grützner, C., Audin, L., Walker, R., ... & Aguirre, E. Did earthquakes strike Machu Picchu?. Journal of Seismology, 24, 883-895, 2020. https://doi.org/10.1007/s10950-019-09877-4

[8] Knudson, C. F. & Perez, V. Accelerograh Records from Lima Peru. 6th World Conference on Earthquake Engineering, India, 1977.

[9] Bui, T. T., Limam, A., Sarhosis, V., & Hjiaj, M. Discrete element modelling of the in-plane and out-of-plane behaviour of dry-joint masonry wall constructions. Engineering Structures, 136, 277-294, 2017. https://doi.org/10.1016/j.engstruct.2017.01.020

[10] Quezada, J. C., Vincens, E., Mouterde, R., & Morel, J. C. 3D failure of a scale-down dry-stone retaining wall: A DEM modelling. Engineering Structures, 117, 506-517, 2016. https://doi.org/10.1016/j.engstruct.2016.03.020

[11] Ita, P., Santa-Cruz, S., Daudon, D., Tarque, N., Párraga, A., & Ramos, V. Out-of-plane analysis of dry-stone walls using a pseudo-static experimental and numerical approach in natural-scale specimens. Engineering Structures, 288, 116153, 2023. https://doi.org/10.1016/j.engstruct.2023.116153

[12] Mentese, V. G., Gunes, O., Celik, O. C., Gunes, B., Avsin, A., & Yaz, M. Experimental collapse investigation and nonlinear modeling of a single-span stone masonry arch bridge. Engineering Failure Analysis, 152, 107520, 2023. https://doi.org/10.1016/j.engfailanal.2023.107520

[13] Galassi, S., Misseri, G., & Rovero, L. Capacity assessment of masonry arches on moving supports in large displacements: Numerical model and experimental validation. Engineering Failure Analysis, 129, 105700, 2021. https://doi.org/10.1016/j.engfailanal.2021.105700

[14] Papadopoulos, K., Vintzileou, E., & Psycharis, I. N. Finite element analysis of the seismic response of ancient columns. Earthquake Engineering & Structural Dynamics, 48(13), 1432-1450, 2019. https://doi.org/10.1002/eqe.3207

[15] Savalle, N., Vincens, E., & Hans, S. Seismic behaviour of dry-stone retaining walls: Experimental and numerical pseudo-static studies. In 10th International Masonry Conference (IMC), Milan, 1030-1045, 2018.

[16] Jean, M., & Moreau, J. J. Unilaterality and dry friction in the dynamics of rigid body collections. In 1st Contact Mechanics International Symposium, 31-48, 1992. https://hal.science/hal-01863710

[17] Jean M., The non-smooth contact dynamics method, Comput. Methods Appl. Mech. Eng. 177 (3–4), 235–257, 1999. https://doi.org/10.1016/S0045-7825(98)00383-1

[18] Dubois, F., Acary, V., & Jean, M. The Contact Dynamics method: A nonsmooth story. Comptes Rendus Mécanique, 346(3), 247-262, 2018. https://doi.org/10.1016/j.crme.2017.12.009

[19] Smoljanović, H., Živaljić, N., Nikolić, Ž., & Munjiza, A. Numerical analysis of 3D dry-stone masonry structures by combined finite-discrete element method. International Journal of Solids and Structures, 136, 150-167, 2018. https://doi.org/10.1016/j.ijsolstr.2017.12.012

[20] Haidar, A., Vincens, E., Dedecker, F., & Plassart, R. FEM–DEM modeling of pseudo static experiments on scaled-down rockfill dams with dry stone pitching. International Journal for Numerical and Analytical Methods in Geomechanics, 47(5), 7, 2023. https://doi.org/10.1002/nag.3492

[21] Cuadros-Rojas, E., Saloustros, S., Tarque, N., & Pelà, L. Photogrammetry-aided numerical seismic assessment of historical structures composed of adobe, stone and brick masonry. Application to the San Juan Bautista Church built on the Inca temple of Huaytará, Peru. Engineering Failure Analysis, 107984, 2024. https://doi.org/10.1016/j.engfailanal.2024.107984

[22] Lourenço, P. B. A user/programmer guide for the micro-modeling of masonry structures. Report 03.21.1.31.35. University of Minho, 1996.

[23] Cundall, P. A., Strack O. D. A discrete numerical model for granular assemblies. geotechnique, vol. 29(1), 47-65, 1979. https://doi.org/10.1680/geot.1979.29.1.47

[24] Santa-Cruz, S., Daudon, D., Tarque, N., Zanelli, C., & Alcántara, J. Out-of-plane analysis of dry-stone walls using a pseudo-static experimental and numerical approach in scaled-down

760 specimens. Engineering Structures, 245, 112875, 2021. https://doi.org/10.1016/j.engstruct.2021.112875

761 [25] Munjiza, A., & Latham, J. P. Comparison of experimental and FEM/DEM results for gravitational
762 deposition of identical cubes. Engineering Computations, 21(2/3/4), 249-264, 2004.
763 https://doi.org/10.1108/02644400410519776

764 [26] Sherzer, G. L., Alghalandis, Y. F., Peterson, K., & Shah, S. Comparative study of scale effect in
765 concrete fracturing via Lattice Discrete Particle and Finite Discrete Element Models. Engineering
766 Failure Analysis, 135, 106062, 2022. https://doi.org/10.1016/j.engfailanal.2022.106062

767 [27] Valente, M., & Milani, G. Advanced numerical insights into failure analysis and strengthening of
768 monumental masonry churches under seismic actions. Engineering Failure Analysis, 103, 410-430,
769 2019. https://doi.org/10.1016/j.engfailanal.2019.05.009

770 [28] Valente, M. Earthquake response and damage patterns assessment of two historical masonry
771 churches with bell tower. Engineering Failure Analysis, 107418, 2023.
772 https://doi.org/10.1016/j.engfailanal.2023.107418

773 [29] Tarque, N., Benedetti, A., Camata, G. & Spacone, E. Alternative approach for reproducing the in-
774 plane behaviour of rubble stone walls. Earthquakes and Structures, 13 (1), 29-38, 2017.
775 https://doi.org/10.12989/eas.2017.13.1.029

776 [30] Gong, F., Wang, Z., Zhou, Y., Wang, J., Yang, L., & Ueda, T. Mesoscale simulation of frost
777 damage to rock material based on Rigid Body Spring Method. Cold Regions Science and Technology,
778 201, 103621, 2022. https://doi.org/10.1016/j.coldregions.2022.103621

779 [31] Stewart, D. E. Rigid-body dynamics with friction and impact. SIAM review, 42(1), 3-39, 2000.
780 https://doi.org/10.1137/S0036144599360110

781 [32] Vlachakis, G., Colombo, C., Giouvanidis, A. I., Savalle, N., & Lourenço, P. B. Experimental
782 characterisation of dry-joint masonry structures: Interface stiffness and interface damping. Construction
783 and Building Materials, 392, 130880, 2023. https://doi.org/10.1016/j.conbuildmat.2023.130880

784 [33] Kartal, M. E., Mulvihill, D. M., Nowell, D., & Hills, D. A. Determination of the frictional
785 properties of titanium and nickel alloys using the digital image correlation method. Experimental
786 Mechanics, 51, 359-371, 2011. https://doi.org/10.1007/s11340-010-9366-y

787 [34] Kim, J., Lorenzoni, F., Salvalaggio, M., & Valluzzi, M. R. Seismic vulnerability assessment of
788 free-standing massive masonry columns by the 3D Discrete Element Method. Engineering Structures,
789 246, 113004, 2021. https://doi.org/10.1016/j.engstruct.2021.113004

790 [35] Gonzalez-Valadez, M., Baltazar, A., & Dwyer-Joyce, R. S. Study of interfacial stiffness ratio of a
791 rough surface in contact using a spring model. Wear, 268(3-4), 373-379, 2010.
792 https://doi.org/10.1016/j.wear.2009.08.022

793 [36] Dassault Systems Simulia. “ABAQUS Rigid Body Definition” in ABAQUS Theory manual, 2023.

794 [37] Dassault Systems Simulia. “ABAQUS Rotation variables” in ABAQUS Theory manual, 2023.

795 [38] Dassault Systems Simulia. “ABAQUS Rotary inertia element” in ABAQUS Theory Manual, 2023.
796
797 [39] Dassault Systems Simulia. “Defining general contact interactions in Abaqus/Explicit” in ABAQUS
798 Theory Manual, 2023.

799 [40] Quezada, J. C., Vincens, E., Mouterde, R., & Morel, J. C. 3D failure of a scale-down dry-stone
800 retaining wall: A DEM modelling. Engineering Structures, 117, 506-517, 2016.
801 https://doi.org/10.1016/j.engstruct.2016.03.020

802 [41] Lemos, J.V. Discrete element modeling of masonry structures. Int. J. Archit. Heritage 1 (2), 190–
803 213, 2007. https://doi.org/10.1080/15583050601176868

[42] Canziani, J. Ciudad y territorio en los Andes: Contribuciones a la historia del urbanismo prehispánico. 2nd Edition. Lima: Pontificia Universidad Católica del Perú. PUCP editorial, 2017. https://doi.org/10.18800/9786124146022

[43] Cárdenas, J., Carlotto, V., Cano V., Flores, T., & Oviedo, M. Estudio geológico y geodinámico de los baluartes en el sitio arqueológico de Saqsaywaman-Cusco. Instituto Geológico Minero y Metalúrgico (INGEMMET) y Universidad Nacional San Antonio Abad del Cusco. First report, 2009. https://hdl.handle.net/20.500.12544/2000

[44] Protzen, J. The Fortress of Saqsa Waman: Was it ever Finished?. Ñawpa Pacha 25/27, 155-175, 1987. https://doi.org/10.1179/naw.1987.25-27.1.004

[45] Alva, J., Ortiz, C., Perez, A., & Soto, J. Mediciones geofísicas en el parque arqueológico de Sacsayhuamán. XIX National Congress of Civil Engineering – Huaráz, 2015.

[46] Alva, J., Ortiz, C., Perez, A., Soto, J., & Riveros G. Análisis dinámico bi-dimensional de amplificación sísmica en el parque arqueológico de Sasayhuamán, Cusco. World Engineering Conference on Disaster Risk Reduction, 2016.

[47] Tarque N., Lai C., Bozzoni F., Miccadei E., Piacentini T., Spacone E. & Camata G. Expected ground motion at historical site of Poggio Picenze, Central Italy, with reference to current Italian Building Code. Journal of Engineering Geology, Volume 166, 8, 100-115, 2013. http://dx.doi.org/10.1016/j.enggeo.2013.09.003

[48] Zora-Carvajal, F. Lluvias originan colapso de muralla de fortaleza de Sacsayhuamán. Andina, Peruvian news agency. Publication date: January 14, 2010.

[49] Combey, A., Audin, L., Benavente, C., Bouysse-Cassagne, T., Marconato, L., & Rosell, L. Evidence of a large “prehistorical” earthquake during Inca times? New insights from an indigenous chronicle (Cusco, Peru). Journal of Archaeological Science: Reports, 34, 102659, 2020. https://doi.org/10.1016/j.jasrep.2020.102659

[50] Barrientos, C. W. Peligro sísmico en la subcuenca del Cusco-2019. Cusco Andean University. Posgrade school, 2021. https://hdl.handle.net/20.500.12557/4718

[51] Noël, J. P., & Kerschen, G. (2017). Nonlinear system identification in structural dynamics: 10 more years of progress. Mechanical Systems and Signal Processing, 83, 2-35. https://doi.org/10.1016/j.ymssp.2016.07.020

[52] Murano, A., Mehrotra, A., Ortega, J., Rodrigues, H., & Vasconcelos, G. Comparison of different numerical modelling approaches for the assessment of the out-of-plane behaviour of two-leaf stone masonry walls. Engineering Structures, 291, 116466, 2023. https://doi.org/10.1016/j.engstruct.2023.116466

[53] Fritsch, E., Sieffert, Y., Algusab, H., Grange, S., Garnier, P., & Daudeville, L. Numerical analysis on seismic resistance of a two-story timber-framed structure with stone and earth infill. International Journal of Architectural Heritage, 2018. https://doi.org/10.1080/15583058.2018.1479804

[54] Beck, S. L., & Ruff, L. J. Great earthquakes and subduction along the Peru trench. Physics of the Earth and Planetary Interiors, 57(3-4), 199-224, 1989. https://doi.org/10.1016/0031-9201(89)90112-X

[55] Alva, J. & Ortiz C. Registros acelerométricos del sismo de Paruro – Cusco del 27 de setiembre de 2014. National University of Engineering, Engineering Civil Faculty, Postgraduate, 2014.

[56] Instituto Geofísico del Perú (IGP) – Centro Geofísico Nacional (CENSIS). Earthquake station Wanchaq Cusco, 2023.

[57] National University of Engineering. Faculty of Civil Engineering. Japan-Peru Center for Earthquake Engineering Research & Disaster Mitigation (CISMID). Station name: Parque de la Reserva (Code: PRQ). Earthquake date: May 31, 1970. Magnitude: 6.6 Mb. Geophysical Institute of Peru (IGP).

[58] Aguilar, Z., Roncal, M., & Piedra, R. Probabilistic seismic hazard assessment in the Peruvian territory. In 16th World Conference on Earthquake, 16WCEE Santiago, Chile, 9-13, 2017.

[59] Oliver-Smith, A. Perú, 31 de mayo, 1970: quinientos años de desastre. Semi-annual magazine of the social studies network on disaster prevention in Latin America , 4, 1994.

[60] Silgado, E. Historia de los sismos más notables ocurridos en el Perú (1513-1974). Newsletter C 3, 1978. https://hdl.handle.net/20.500.12544/251

[61] Rosell, L. N., Benavente, C. L., Aguirre, E. M., Fernández, B. G., & Palomino, A. R. Expresión geomorfológica de tectónica activa y paleosismología en el Cusco: caso falla Tambomachay-[Bulletin C 88], 2022. https://hdl.handle.net/20.500.12544/3598